Nano Energy (2015) 12, 510–520

Available online at www.sciencedirect.com

ScienceDirect

journal homepage: www.elsevier.com/locate/nanoenergy

RAPID COMMUNICATION

Ultrathin MoO_3 nanocrystalsself-assembled on graphene nanosheets via oxygen bonding as supercapacitor electrodes of high capacitance and long cycle life

Kai Zhou[a], Weijia Zhou[a,*], Xiaojun Liu[a], Yuanhua Sang[b], Shaozheng Ji[b], Wei Li[a], Jia Lu[a], Ligui Li[a], Wenhan Niu[a], Hong Liu[b], Shaowei Chen[a,c,*]

[a]*New Energy Research Institute, School of Environment and Energy, South China University of Technology, Guangzhou Higher Education Mega Center, Guangzhou, Guangdong 510006, China*
[b]*State Key Laboratory of Crystal Materials, Center of Bio & Micro/Nano Functional Materials, Shandong University, 27 Shandanan Road, Jinan, Shandong 250100, China*
[c]*Department of Chemistry and Biochemistry, University of California, 1156 High Street, Santa Cruz, CA 95064, USA*

Received 22 October 2014; received in revised form 16 December 2014; accepted 8 January 2015
Available online 16 January 2015

KEYWORDS
MoO_3;
3D graphene frameworks;
Oxygen-bonding;
Solid-state symmetric supercapacitor;
Electrochemical stability

Abstract
Ultrathin MoO_3 nanocrystals were assembled on 3D graphene oxide frameworks via a hydrothermal reaction forming a layered structure by oxygen-bonding interactions at the interface. The structure and morphology of the resulting MoO_3-GAs hybrids were characterized by a range of experimental tools including atomic force microscopy, scanning electron microscopy, transmission electron microscopy, X-ray photoelectron spectroscopy, infrared and Raman spectroscopy. Because of abundant exposed active sites of the ultrathin MoO_3 and rapid ion diffusion and electron transport of 3D graphene frameworks, the resulting MoO_3-GAs hybrids possess the highest specific capacitances and excellent cycling stability in both aqueous (527 F g^{-1} at the current density of 1.0 A g^{-1}, 100% retention after 10,000 cycles) and solid electrolytes (373 F g^{-1} at 1.0 A g^{-1}, 100% retention after 5,000 cycles) among leading literature results of similar systems.

*Corresponding authors.
E-mail addresses: eszhouwj@scut.edu.cn (W. Zhou), shaowei@ucsc.edu (S. Chen).

http://dx.doi.org/10.1016/j.nanoen.2015.01.017
2211-2855/

Introduction

Supercapacitors are a promising class of energy storage devices due to their high power density, ultrafast charging/discharging rate and excellent cycle performance, which show potential applications for hybrid electric vehicles, consumer electronics, backup energy systems, etc [1-4]. In recent years, extensive research has been devoted to the design and engineering of new materials and structures to further improve their electrochemical performance, for instance, using pseudocapacitors which store charges through fast reversible Faradaic reactions from redox-active materials [5-7]. Among these, layered transition metal oxides/hydroxides, such as MnO_2 [8], $Co(OH)_2$ [9], V_2O_5 [10], and $Ni(OH)_2$ [11], have been extensively explored as supercapacitor electrodes for the enhancement of specific capacitance, energy and power density.

In particular, α-MoO_3 is an n-type semiconductor with an anisotropic layered structure along the [0 1 0] direction. The layered structure is formed by stacking bilayer sheets of MoO_6 octahedra with van der Waals forces [12,13]. These structures are presumably advantageous for the insertion/removal of small ions such as H^+ and K^+. However, its low electronic conductivity and lack of structural integrity under electrochemical reactions are detrimental to a high-rate and long-term cycling performance in electrochemical devices [14-16]. Therefore, it remains a challenge to use MoO_3 as supercapacitor electrodes, because the capacitance may diminish significantly in a prolonged charge–discharge cycling process. For example, Kim et al. reported that the capacitance of structured MoO_3 diminished by 18% after only 1000 cycles of charging and discharging [17]. Li et al. also reported a significant loss of 25% of the capacitance of α-MoO_3 after only 1000 cycles [18]. This is the primary motivation of the present study in which we employ two effective strategies to overcome this attenuation problem: (i) fabrication of ultrathin MoO_3 nanocrystals on the surface of mechanically robust graphene nanosheets leading to a high electrochemically active surface area for faradic reactions at the defects and grain boundaries of the crystalline lattices, and (ii) formation of strong chemical contacts between the ultrathin MoO_3 nanocrystals and graphene via oxygen bonding to facilitate interfacial charge transfer and to reduce the loss of active materials.

Graphene with large specific surface area, high electrical conductivity, excellent mechanical properties and chemical stability, has shown great potential for supercapacitor electrode materials [19-22]. However, because of easy restacking of the graphene nanosheets due to strong π-π interactions, supercapacitor electrodes based directly on graphene sheets did not display the expected high rate performance. A variety of three-dimensional (3D) graphene materials, for example, graphene hydrogels [23-26] and graphene papers [27-28], which contain continuously interconnected pores structures with high surface area-to-volume ratios have been developed to overcome the restacking problems of graphene sheets. At the same time, due to their outstanding electrical properties and mechanical flexibility, monolithic 3D graphene has been widely explored as electrode materials for solid-state supercapacitors, which are considered as promising smart and efficient energy-storage devices [24,29,30].

In this work, ultrathin MoO_3 nanocrystals were epitaxially grown on the surface of graphene oxide (GO) nanosheets that self-assembled into 3D aerogels (MoO_3-GAs). A variety of experimental techniques including atomic force microscopy (AFM), transmission electron microscopy (TEM), X-ray photoelectron spectroscopy (XPS), infrared and Raman spectroscopy were used to characterize the resulting composite structure and interfacial bonding between the MoO_3 nanocrystals and graphene nanosheets. Electrochemical studies showed that MoO_3-GAs might be used as effective supercapacitor electrodes with an excellent specific capacitance of 586 F g^{-1} at the scan rate of 50 mV s^{-1} and 527 F g^{-1} at the current density of 1.0 A g^{-1} in 1.0 M H_2SO_4 aqueous electrolyte in a three-electrode configuration. Remarkably, the electrode materials also exhibited excellent stability in long-term cycling in both aqueous (at a current density of 10.0 A g^{-1}, 100% retention after 10,000 cycles) and solid electrolytes (at a current density of 1.0 A g^{-1}, 100% retention after 5000 cycles). To our knowledge, this is the best supercapacitor performance, in particular, with regard to specific capacitance and cycling stability, as compared to those reported in the literature of Mo-based supercapacitor electrode materials.

Experimental section

Materials

Sodium molybdate ($Na_2MoO_4 \cdot 2H_2O$), graphite powers, potassium persulfate ($K_2S_2O_8$), phosphorus pentoxide (P_2O_5), potassium permanganate ($KMnO_4$), hydrogen peroxide (H_2O_2) and dimethylformamide (DMF) were purchased from Sinopharm Chemical Reagents Co., Ltd. All reagents were of analytical grade, and used without further purification. Deionized water was supplied with a Barnstead Nanopure Water System (18.3 MΩ cm).

Synthesis of MoO_3-GAs

Graphene oxide (GO) was prepared by a modified Hummers method using natural graphite flakes as the starting materials [31]. MoO_3-graphene aerogels (MoO_3-GAs) were synthesized by a combined hydrothermal and freeze-drying method. In a typical procedure, 15 mL of a GO (4.0 mg mL^{-1}) solution in DMF containing 50 mg of sodium molybdate was dispersed evenly by ultrasonic agitation to obtain an emulsion. The resulting dispersion was sealed in a Teflon-lined autoclave, and heated at 200 °C for 24 h. After the autoclave naturally cooled to room temperature, the as-prepared graphene hydrogel was taken out and cleaned with deionized water several times until the solution became clear, followed by freeze-drying at −45 °C for 24 h. For comparison, pristine graphene oxide aerogels (GAs), and MoO_3-GAs at other MoO_3 loadings were also prepared in a similar fashion with GO solution: 10 mg of sodium molybdate to prepare a lower MoO_3 loading of MoO_3-GAs (L-MoO_3-GAs), and 100 mg to a higher MoO_3 loading sample (H-MoO_3-GAs).

Structural characterizations

The microstructural and morphological details of the samples were examined with a NOVA NANOSEM 430 field emission

scanning electron microscope (FESEM) and a JEOL JEM-2100 transmission electron microscope (TEM) at an acceleration voltage of 200 kV. AFM measurements were performed using a Nanosurf Easyscan2 instrument (Veeco Dimension 3100). The MoO_3-GAs was dispersed in ethanol by ultrasonic agitation to obtain homogeneously dispersed MoO_3-graphene nanosheets, which were dropped onto the surface of a clean silicon wafer. Chemical compositions were evaluated by element mapping (Philips Tecnai F20) and XPS (ESCALAB 250) measurements. XRD analysis was performed on a Bruker AXS D8 Discover diffractometer with Cu $K\alpha$ radiation. Raman spectra were recorded on a RENISHAW inVia instrument with an Ar laser source of 488 nm in a macroscopic configuration. Infrared spectra were acquired with a NICOLET 6700 FTIR spectrometer (Thermo Scientific, USA). The BET surface area was characterized by Micromeritics ASAP 2010 with nitrogen adsorption at 77 K. Thermogravimetric analyses (TGA) was carried out under a steady flow of O_2, where the temperature was scanned from 30 to 600 °C at a rate of 10 °C min^{-1}.

Electrochemical measurements

The monolithic aerogels were cut into small slices with a thickness of about 1 mm and diameter of about 10 mm, which were further pressed onto titanium meshes as working electrodes. All electrochemical experiments were carried out with a CHI 660E Electrochemical Workstation (CH Instruments, China). In the three-electrode system, a saturated calomel reference electrode (SCE, Hg/Hg_2Cl_2 in saturated KCl) and a Pt counter electrodes were used along with 1.0 M H_2SO_4 aqueous electrolyte. In the two-electrode system, two same slices of the aerogel monoliths that were pressed on titanium meshes were directly assembled into a symmetric supercapacitor in 1.0 M H_2SO_4 aqueous electrolyte. In the case of solid-state symmetric supercapacitors, two slices of aerogel monoliths pressed on titanium meshes were immersed in the solution of PVA/H_2SO_4 gel electrolyte for several times. The resulting electrolyte-filled electrodes were solidified for 12 h at ambient conditions. Finally, the two electrodes were assembled into a solid-state symmetric supercapacitor carefully. The gel electrolyte was fabricated by mixing 3 g H_2SO_4 and 3 g PVA in 30 mL of deionized water that was subject to heating up to 80 °C for several hours under vigorous stirring until the solution become transparent.

Specific capacitance C (F/g) for a single electrode was calculated from the CV and charge-discharge curves by Eqs. (1) and (2), respectively, where I_1 (A) is the response current, ΔV (V) is the voltage window, ν (V/s) is the scan rate, I_2 (A) is the constant discharge current, Δt (s) is the discharging time and m_1 (g) is the weight of the single electrode.

$$C = \frac{\int I_1 dV}{\nu m_1 \Delta V} \tag{1}$$

$$C = \frac{I_2 \Delta t}{m_1 \Delta V} \tag{2}$$

Energy density (E) and power density (P) were calculated by Eqs. (3) and (4), respectively.

$$E = \frac{1}{2} C(\Delta V)^2 \tag{3}$$

$$P = \frac{E}{\Delta t} \tag{4}$$

Specific capacitance C_s (F/g) for symmetric supercapacitor was calculated from the CV and charge-discharge curves by Eqs. (5) and (6), respectively, where I_1 (A) is the response current, ΔV (V) is the voltage window, ν (V/s) is the scan rate, I_2 (A) is the constant discharge current, Δt (s) is the discharging time and m_2 (g) is the total mass of two electrodes.

$$\frac{C_s = 4\int I_1 dV}{\nu m_2 \Delta V} \tag{5}$$

$$C_s = \frac{4 I_2 \Delta t}{m_2 \Delta V} \tag{6}$$

Result and discussion

As manifested in SEM studies (Figure 1a and b), the as-prepared MoO_3-GAs exhibited a 3D interconnected porous network with a smooth surface, where graphene sheets most likely served as the structural scaffolds. Note that MoO_3-GAs might be exfoliated and dispersed in ethanol by ultrasonic agitation forming a homogeneous solution of MoO_3/graphene nanosheets. AFM topographic studies showed that the height of the MoO_3/graphene nanosheets was rather uniform at <2.0 nm (Figure 1c and **S1**), signifying that MoO_3 were likely evenly distributed on the surface of the graphene nanosheets which served as a structural unit in the MoO_3-GAs hybrids (vide infra). Note that the resolution of SEM and AFM were not high enough to identify the exact location of the MoO_3 nanocrystals (MoO_3 was not detected in XRD measurements either, because of small size and low loading, Figure S2a). A broad diffraction peak centered at around 24.5° in Fig. S2a was ascribed to the graphite (0 0 2), because of reduction of oxygen functional groups in graphene [24,32]. However, the XRD pattern of H-MoO_3-GAs in Figure S2b exhibted three diffraction peaks at 2θ=12.8°, 25.7° and 39.0°, characteristic of the (0 2 0), (0 4 0) and (0 6 0) diffraction planes of MoO_3 (JCPDS no. 05-0508), respectively. Then, the loading amount of MoO_3 was measured by TGA measurements (Figure S3). It can be seen that the MoO_3 loading was quantified at 4.8 wt%, 18.6 wt%, 30.8 wt% of for L-MoO_3-GAs, MoO_3-GAs and H-MoO_3-GAs, respectively.

The formation of MoO_3-GAs composites was readily manifested in FTIR measurements, as depicted in Figure 1d. It can be seen that several prominent vibrational bands appear at 1571 cm^{-1}, 1401 cm^{-1}, and 1180 cm^{-1} with both MoO_3-GAs (black curve) and pristine GAs (red curve). These may be assigned to the C=C, C−C and C−O functional moieties of the graphene nanosheets, respectively. For the MoO_3-GAs composites, however, several additional virbational bands emerged within the range of 500-1000 cm^{-1}. Of these, the vibrational bands at 945 cm^{-1} and 896 cm^{-1} might be assigned to the Mo-terminal oxygen stretching vibrations, while the peaks at 616 cm^{-1} and 779 cm^{-1} were likely due to the stretching vibrations of oxygen linked with two or three molybdenum atoms, respectively [16,33,34]. Consistent results were obtained in Raman measurements, as depicted in the inset to Figure 1d. One can see that after MoO_3 was deposited onto the

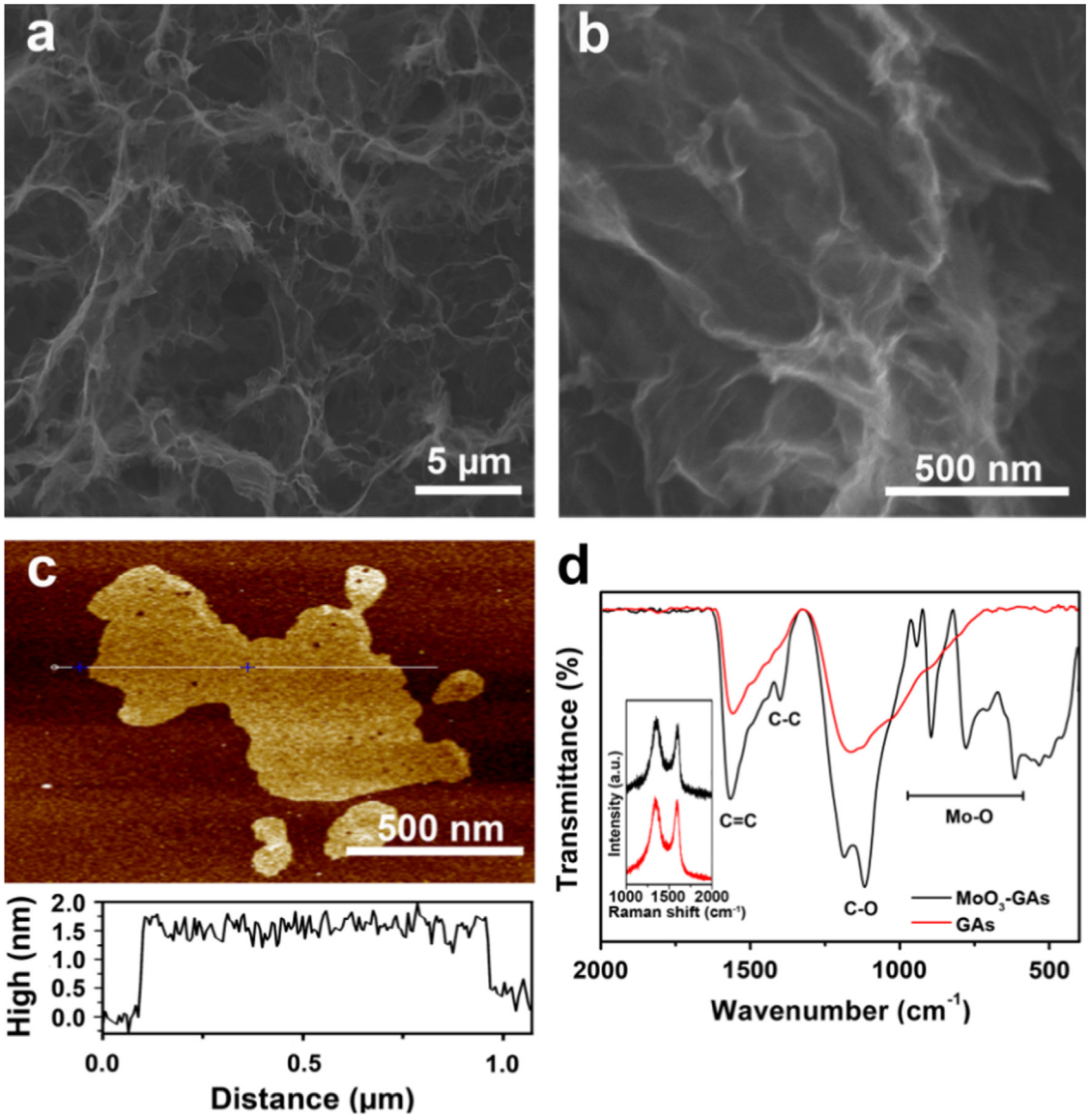

Figure 1 (a) and (b) SEM images of MoO_3-GAs. (c) Representative AFM topograph of MoO_3/graphene nanosheets and the corresponding line-scan profile. (d) FTIR spectra of the pristine GAs and MoO_3-GAs. Inset is the corresponding Raman spectra.

graphene sheets (black curve), the graphene D and G bands red-shifted somewhat to 1352 and 1589 cm^{-1} from 1344 and 1584 cm^{-1} of the pristine graphene areogels (GAs, red curve), along with an increase of the ratio of the their intensities (I_D/I_G) to 1.14 from 1.05. This may be accounted for the enhanced defect structures of the graphene nanosheets upon the loading of MoO_3 [35].

Further morphological details were resolved in (HR)TEM analyses, which provided direct evidence of ultrathin MoO_3 nanocrystals self-assembled on graphene oxide nanosheets. Figure 2a and b shows that the MoO_3/graphene nanosheets exhibited a highly wrinkled surface; and MoO_3 nanocrystals can be seen to be rather evenly distributed on the surface of the graphene nanosheets, as manifested in high-resolution measurements (Figure 2c) where well-defined lattice fringes can be resolved and the interplanar spacing of 0.38 nm is consistent with the (1 1 0) crystalline planes of MoO_3 that were perpendicular to the graphene nanosheets. These observations were in good agreement with results in AFM study (Figure 1c). The crystalline properties of the composites were also examined by selected area electron diffraction (Figure S4) that clearly signified the formation of polycrystalline MoO_3 nanocrystals on graphene nanosheets. Note that MoO_3 is a layered semiconductor with an anisotropic layered structure along the [0 1 0] direction (Figure 2d). The layered structure is formed by stacking bilayer sheets of MoO_6 octahedra by van der Waals forces [36,37]. The thickness of a single layer of MoO_6 octahedra is about 0.7 nm, and a MoO_3/graphene sheet/MoO_3 sandwich structure is about 1.7 nm in thickness. This is in good agreement with the thickness determined by AFM measurements of the MoO_3/graphene nanosheet composites (Figure 1c), suggesting the formation of MoO_3/graphene/MoO_3 sandwiched structures. Furthermore, elemental mapping studies of the MoO_3-graphene composites showed a uniform

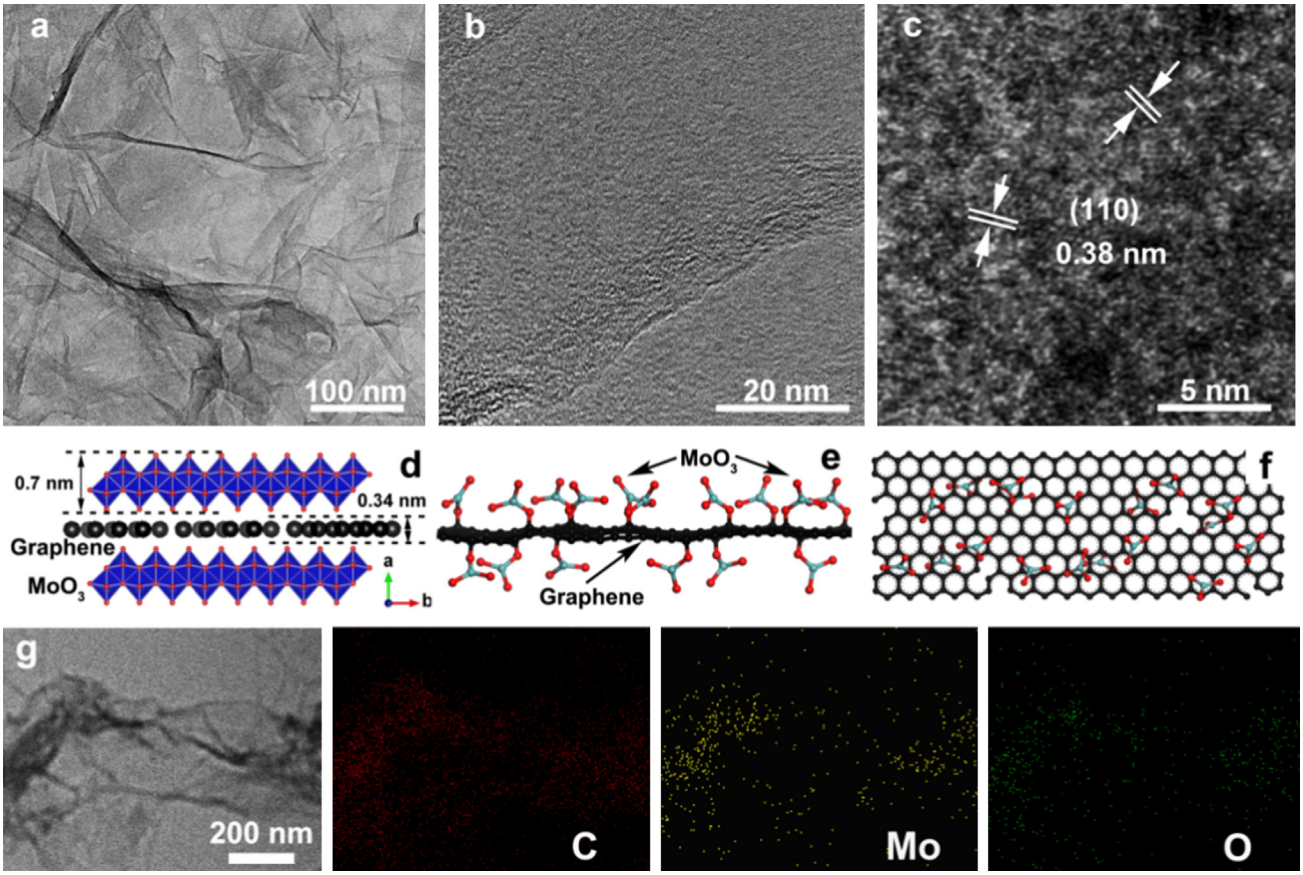

Figure 2 (a) Low and (b) high resolution TEM images of the MoO_3/graphene nanosheets. (c) STEM image of MoO_3/graphene nanosheets. (d) Schematic of MoO_3 self-assembled on graphene nanosheets. (e) and (f) Schematic diagrams of MoO_3 bonding with graphene. (g) Element mapping images of MoO_3-graphene nanosheets.

distribution of the C, Mo, and O elements (Figure 2g), consistent with results from SEM (Figure 1b), AFM (Figure 1c) and HRTEM (Figure 2b and c) measurements.

XPS measurements were then carried out to characterize the surface elemental compositions and valence states of the MoO_3-GAs. As shown in the survey spectrum in Figure 3a, carbon, molybdenum and oxygen were the only elements that could be identified. Deconvolution of the high-resolution scan of the C1s electrons exhibited three peaks at 284.5, 285.5 and 290.2 eV (Figure 3b), corresponding to the C=C, C−O and O=C−OH carbons, respectively [38]. This suggests the formation of oxygenated functional moieties in graphene oxide nanosheets. For the Mo3d electrons (Figure 3c), a doublet can be identified at 235. 6 eV and 232.5 eV, in good agreement with the binding energies of the Mo (VI) $3d_{3/2}$ and $3d_{5/2}$ electrons and hence the formation of MoO_3 in the composites [37]. For the O1s electrons (Figure 3d), two components can be deconvoluted: O1 at the low binding energy of 530.4 eV which might be assigned to the lattice oxygen in MoO_3, whereas the peak at 532.4 eV (O2) to C−O of graphene oxide [38,39]. In addition, the survey spectrum of bare GAs was showed in Figure S5a, where carbon and oxygen were the only elements that could be identified. Deconvolution of the high-resolution scan of the O1s electrons exhibited two peaks at 531.1 and 532.4 eV (Figure S5b), corresponding to the C=O and C−O of graphene oxide, respectively [38]. These comparisons suggest the replacement of C=O by Mo in MoO_3 forming the C−O−Mo linkage. Therefore, we concluded that the self-assembly of ultrathin MoO_3 nanocrystals on graphene oxide nanosheets were facilitated via oxygen-bonding interactions (C−O−Mo) at the interface. Furthermore, based on the integrated peak areas, the atomic ratio of Mo/C in MoO_3-GAswas estimated to be only 2.6 at%, corresponding to a mass loading of MoO_3 in MoO_3-GAs at 23.7 wt%. Two additional MoO_3-GAs hybrids were prepared in a similar fashion with the corresponding mass contents of MoO_3 at about 4.9 wt% (L-MoO_3-GAs) and 33.8 wt% (H-MoO_3-GAs), respectively, as shown in Figure S6. The results of MoO_3 loading estimated from XPS were consistent with those obtained by TGA (Figure S3).

In order to further study the assembly mechanism between MoO_3 and graphene nanosheets, a reduced graphene/MoO_3 composite (RGO-Mo) was synthesized in the same manner except that reduced graphene oxide prepared by chemical reduction with hydrazine hydrate was used instead of graphene oxide (synthetic details in the Supporting Information). As shown in Figure 4a and b, molybdenum could not be detected in RGO-Mo (red curve), whereas Mo3d and Mo3p were very well-defined in MoO_3-GAs (black curve). This indicated that MoO_3 nanocrystals could not be formed on reduced graphene without dangling oxygen in DMF hydrothermal reaction. Further studies showed that no MoO_3 nanocrystals were produced in the absence of graphene oxide nanosheets in DMF hydrothermal reaction (Figure S7). Therefore, it is likely that the oxygenated moieties on the

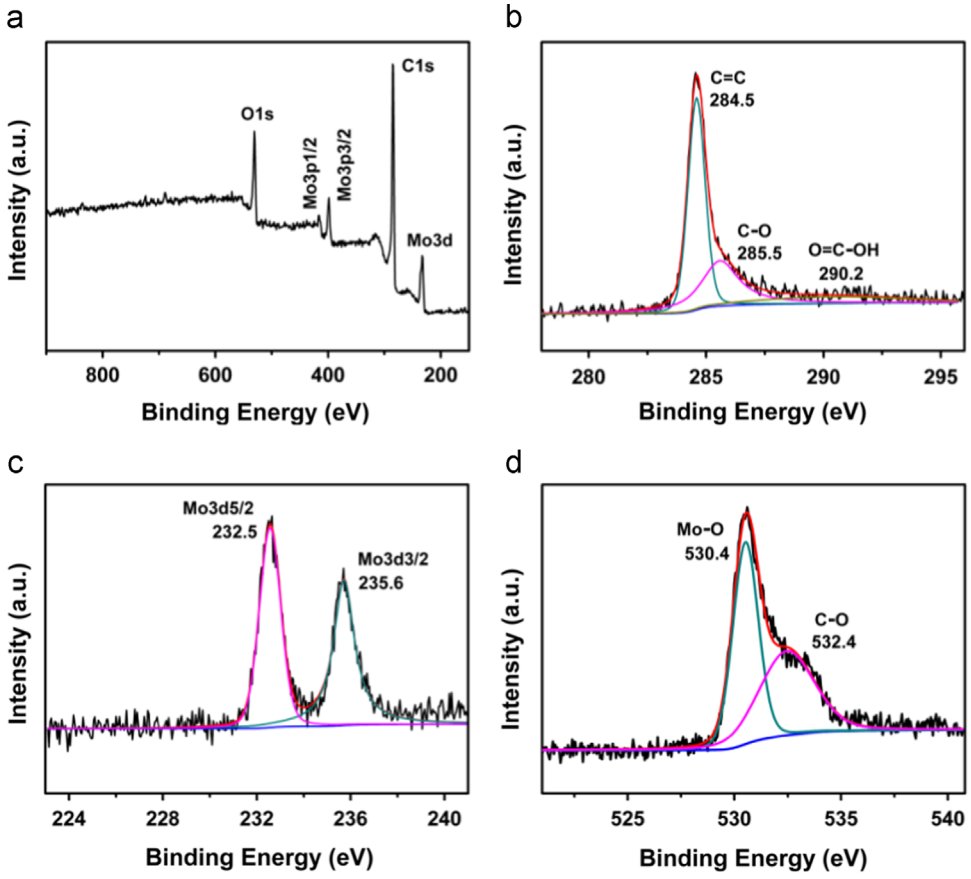

Figure 3 (a) XPS survey spectrum of MoO_3-GAs and high resolution scans of (b) C1s, (c) Mo3d and (d) O1s electrons. Black curves are experimental data and color curves are deconvolution fits.

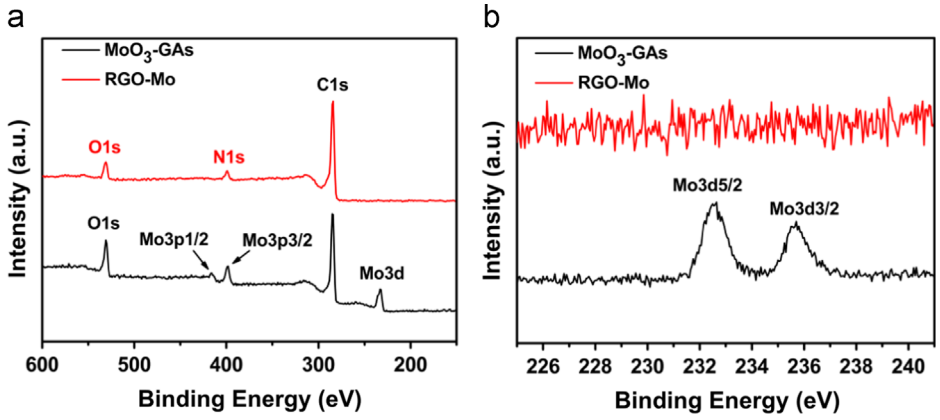

Figure 4 (a) XPS survey spectra of MoO_3-GAs and RGO-Mo. (b) High resolution scans of the Mo3d electrons of MoO_3-GAs and RGO-Mo.

graphene oxide nanosheets played an important role in the assembly of ultrathin MoO_3 nanocrystals by Mo—O—C bonding linkages at the interface. On the basis of these XPS results (Figs. 3 and 4), the oxygen-bonding structures between graphene oxide and MoO_3 were depicted in Figure 2e and f. Note that similar structures have been reported previously, such as Ni $(OH)_2$/graphene [38] and MoS_2/graphene [40], where it was reported that oxygen on graphene might affect the structure and morphology of the resulting composites.

Remarkably, the prepared MoO_3-GAs composites exhibited a significant performance as supercapacitor electrodes. Cyclic voltammetry (CV) and galvanostatic charge/discharge were employed to examine the electrochemical properties of MoO_3-GAs electrodes in an aqueous electrolyte of 1.0 M H_2SO_4 in a three-electrode (Figure 5) and two-electrode configuration (Figure S8). For comparison, pristine GAs and MoO_3 were also tested under the same conditions. Figure 5a shows the CV curves of the GAs and MoO_3-GAs electrodes at the scan rate of 50 mV s^{-1}. It can be seen that the GAs exhibits a typical rectangular shape (black curve), implying pure electrical double-layer capacitive behaviors. In contrast, MoO_3-GAs displays two pairs of rather well-defined voltammetric peaks (red

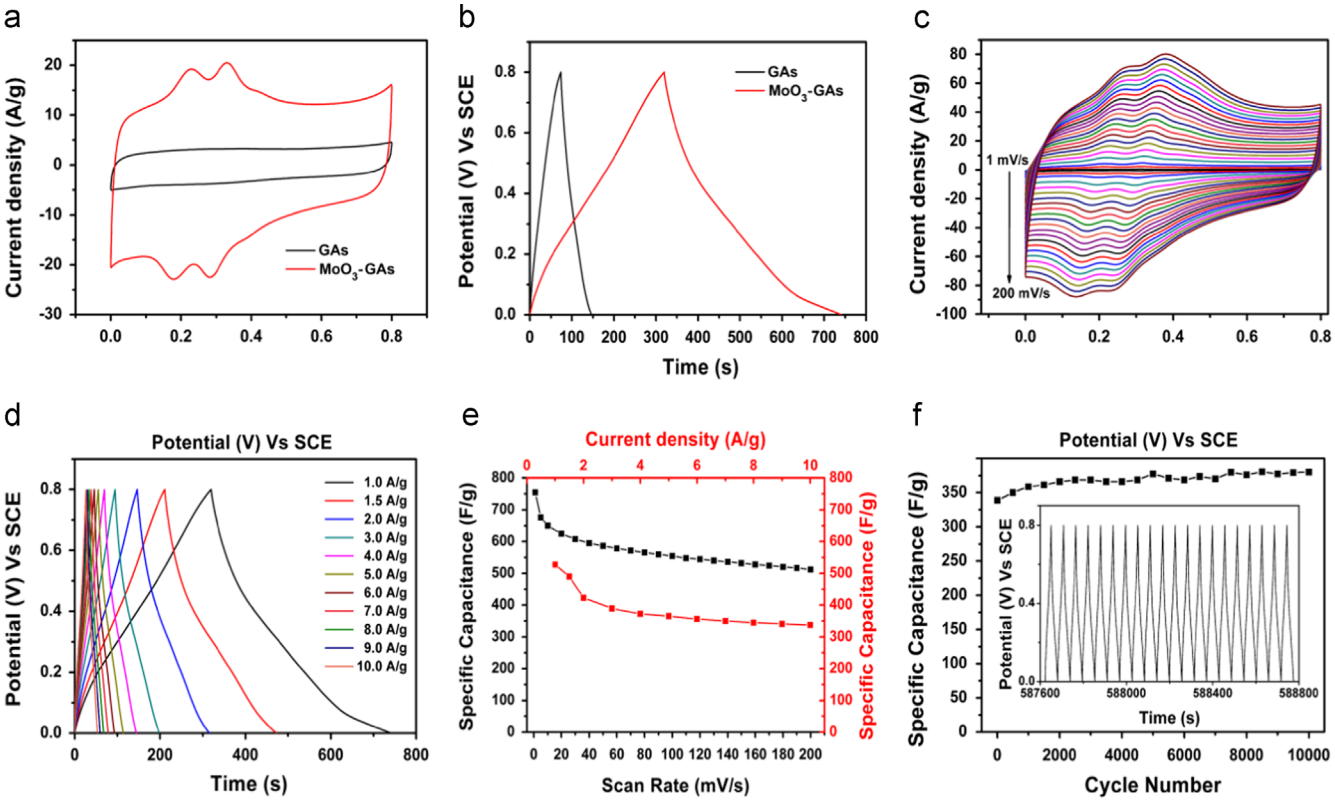

Figure 5 (a) CV curves of GAs and MoO_3-GAs electrodes at the scan rate of 50 mV s^{-1}. (b) Galvanostatic charge/discharge curves at a current density of 1 A g^{-1}. (c) CV curves of the MoO_3-GAs electrode at different scan rates in 1.0 M H_2SO_4. (d) Galvanostatic charge/discharge curves of the MoO_3-GAs electrode at different current densities. (e) Specific capacitance of the MoO_3-GAs electrode as a function of scan rate and current density. (f) Cycling stability of the MoO_3-GAs electrode at a current density of 10.0 A g^{-1}. Inset is the last 20 charge/discharge profile of the MoO_3-GAs at 10.0 A g^{-1}.

curve) with the formal potentials ($E^{\circ\prime}$) at +0.20 V and +0.30 V, respectively, which might be ascribed to the redox reactions of Mo(VI)↔Mo(V)↔Mo(VI) [18]. Similar results were obtained in CV measurements of pristine MoO_3 (Figure S9). Such voltammetric features have also been observed in Li-ion batteries with a MoO_3 electrode [16,41]. In addition, the peak splitting (ΔE_p) of the two pairs of voltammetric peaks was only 5.1 mV and 4.8 mV indicating facile electron-transfer kinetics, which is advantageous for pseudo-capacitive contributions. Importantly, from these CV profiles, the MoO_3-GAs composites showed an impressive specific capacitance of 586 F g^{-1} at the scan rate of 50 mV s^{-1}, more than 5-fold larger than that of GAs (122 F g^{-1}), and markedly higher than that of pristine MoO_3 (1.7 F g^{-1}). Furthermore, in the galvanostatic charge/discharge measurements (Figure 5b), pristine GAs exhibited a rather symmetrical triangular shape (black curve) whereas marked deviation can be seen with MoO_3-GAs (red curve), as a result of significant contributions of faradaic capacitance, as described above. The specific capacitance of MoO_3-GAs was estimated to be 527 F g^{-1} at the current density of 1.0 A g^{-1}, while that of GAs was only 91 F g^{-1}. It is worth noting that when normalized to the mass of redox-active MoO_3 alone the specific capacitance of MoO_3-GAs was actually 2223.6 F g^{-1} at 1.0 A g^{-1}.

As shown in Figure 5c, the voltammetric features of the MoO_3-GAs electrode remained virtually unchanged with the potential scan rate varied from 1.0 to 200 mV s^{-1}, consistent with fast electron-transfer kinetics. This was further supported by results from electrochemical impedance analysis (Figure S10). The equivalent series resistance (ESR) of MoO_3-GAs was only 1.4 Ω, close to that of pure GAs (1.2 Ω); and the deposition of MoO_3 nanocrystals on the graphene oxide surface did not appear to affect charge diffusion, as manifested by the similar slope of the low-frequency linear segment of MoO_3-GAs and pure GAs. Nevertheless, the arc in the high frequency region exhibits a larger diameter with MoO_3-GAs than with GAs alone, which might be ascribed to the redox reactions of ultrathin MoO_3 nanocrystals deposited on the graphene oxide surface in MoO_3-GAs.

Figure 5d depicted the galvanostatic charge/discharge curves of the MoO_3-GAs electrode in 1.0 M H_2SO_4 aqueous electrolyte at different current densities. The specific capacitances were calculated by the integrated area of the CV curves and discharging time of the galvanostatic charge/discharge curves, respectively. The correlation between the specific capacitance and the scan rate and current density for the MoO_3-GAs electrode was presented in Figure 5e. Notably, the specific capacitance of MoO_3-GAs showed only a slight decrease to 512 F g^{-1} at a scan rate of 200 mV s^{-1} from 755 F g^{-1} at 1.0 mV s^{-1}. Furthermore, with the increase of the current density up to 10.0 A g^{-1}, the specific capacitance of MoO_3-GAs remains at 328 F g^{-1}. The excellent rate capability of the MoO_3-GAs electrode could be ascribed to the efficient, fast charge transport of the 3D graphene frameworks.

The electrochemical stability of the MoO_3-GAs electrode was also investigated by galvanostatic charge/discharge

measurements at a high current density of 10.0 A g^{-1} (Figure 5f). The specific capacitance increased slightly at the early stage of cycling (up to 1000 cycles), which may be ascribed to the repetitive charging/discharging cycles that improved ion accessibility in MoO_3-GAs, leading to increased accommodation for ions, as reported previously [42]. Remarkably, the specific capacitance remained almost invariant at about 380 F g^{-1} even after 10,000 cycles of charging and discharging. This was in sharp contrast with pristine MoO_3 where only 58.7% of the initial capacitance was retained even at 0.05 A g^{-1} over 600 cycles (Figure S9d). This result indicated that the 3D graphene frameworks allowed for large strain accommodation during the ion insertion/removal process, and the interactions between MoO_3 and graphene were strong enough to sustain a long cycle life. In order to demonstrate this deduction, SEM, TEM and Raman analysis of the used MoO_3-GAs electrode after cycling performance have been accomplished. As shown in Figure S11a-b, it can be clearly observed that there was almost no change of the morphology. The nanostructure of used electrode did not present microstructural agglomeration or pulverization issue. MoO_3 nanocrystals still can be seen to be rather evenly distributed on the surface of the graphene nanosheets, as manifested in high-resolution measurements (Figure S11c). Consistent results were obtained in Raman measurements, as depicted in Figure S11d, two apparent vibrational bands can beidentified at 1352 and 1589 cm^{-1}, and the I_D/I_G remained almost invariant after charging and discharging cycles testing.

The energy and power density of MoO_3-GAs electrode were evaluated by the Ragone plots calculated from galvanostatic charge/discharge curves (Figure S12). The MoO_3-GAs electrode in 1.0 M H_2SO_4 aqueous solution delivered a high energy density of 62 W h kg^{-1} at a power density of 320 W kg^{-1}, and still remained at 30 W h kg^{-1} at a power density of 4000 W kg^{-1}. It should be noted that this excellent capacitance performance (527 F g^{-1} at the current density of 1.0 A g^{-1}, which remained unchanged after 10,000 cycles) of MoO_3-GAs is the best among literature results with supercapacitors based on graphene (or carbon nanotubes) and MoO_3 electrodes (Table 1), such as RGO/α-MoO_3 (291 F g^{-1} at 2 mV s^{-1}, no result for cycling stability) [14], MoO_3/SWNT (540 F g^{-1} at 0.1 mV s^{-1}, no result for cycling stability) [43], MoS_2/RGO (265 F g^{-1} at 10 mV s^{-1}, 97% retention after 1000 cycles) [40], MoO_3 hybrids (135 F g^{-1} at 1.3 A g^{-1}, 82% retention after 1000 cycles) [17], and MoO_3/MWCNT (103 F g^{-1} at 25 mV s^{-1}, 80% retention after 1000 cycles) [15].

CV measurements of the hybrid materials at different mass loading of MoO_3 were also carried out. As shown in Figure S13a and b, the L-MoO_3-GAs (4.9 wt% by XPS) electrode exhibited a specific capacitance of 321 F g^{-1} at the scan rate of 50 mV s^{-1}, lower than that of MoO_3-GAs (23.7 wt%, 586 F g^{-1}). For H-MoO_3-GAs (33.8 wt% by XPS), the initial specific capacitance was 554 F g^{-1} at the scan rate of 50 mV s^{-1}, but the cycling stability was rather poor as the specific capacitance diminished to 323 F g^{-1} after only 100 cycles. The same cycling stability was also demonstrated by charge-discharge cycles testing (Figure S14). According to the structure and morphology of H-MoO_3-GAs (Figure S13c and d), two kinds of MoO_3 (ultrathin nanocrystals and large particles) were on the surface of graphene in H-MoO_3-GAs. The poor cycling stability of H-MoO_3-GAs is possibly due to the large size and mass loss of the latter large MoO_3 particles on the reduced graphene oxide surface. These results indicate that the mass loading and existence form of MoO_3 on reduced graphene oxide surface is important in the determination of the capacitance performance.

The remarkable supercapacitor performance of MoO_3-GAs might be accounted for the following factors. Ultrathin MoO_3 nanocrystals facilitated fast and reversible redox reactions, with improved rate capability, and the stacking of monolayers of MoO_6 octahedra on graphene nanosheets that was advantageous to insertion/removal of small ions such as H^+ and K^+. Usually, a large resistance occurred when the H^+ and K^+ ions were inserted into multilayers and blocks of layered compounds that may cause structural fatigue of the materials. In the present study, ultrathin MoO_3 nanocrystals were assembled onto graphene nanosheets via strong oxygen-bonding interactions where ion diffusion was facilitated by the highly porous structures and electron transport effected by the Mo—O—C interfacial bonding linkages, as manifested by the high electrical conductivity and specific surface area (154.6 m^2 g^{-1}, Figure S15) of 3D graphene frameworks [44,45].

The as-obtained MoO_3-GAs can be cut into small pieces with good mechanical flexibility. These may then be assembled into a solid-state symmetric supercapacitor using a gel electrolyte (Figure 6a). The electrochemical performance of the as-fabricated devices was shown in Figure 6b-f. The almost rectangular CV curves and triangular galvanostatic charge-discharge curves of the device in Figure 6b and c demonstrate a typical capacitive behavior. As shown in Figure 6d, the MoO_3-GAs based device delivered a specific capacitance of 373 F g^{-1} at 1.0 mV s^{-1} and 181 F g^{-1} at 100 mV s^{-1}. The excellent performance of MoO_3-GAs could be attributed to the unique structural

Table 1 Summary of supercapacitor performance of graphene (or carbon nanotubes) and Mo based supercapacitor electrodes in a three-electrode configuration.

Electrode materials	Electrolyte	Specific capacitance	Cycling stability	References
MoO_3-GAs	1 M H_2SO_4	755 F g^{-1} at 1.0 mV s^{-1}	10,000 (100%)	This work
RGO/α-MoO_3	1 M Na_2SO_4	291 F g^{-1} at 2 mV s^{-1}	No result	14
MoO_3/SWNT	1 M $LiClO_4$ propylene carbonate	540 F g^{-1} at 0.1 mV s^{-1}	No result	43
MoS_2/RGO	1 M $HClO_4$	265 F g^{-1} at 10 mV s^{-1}	1000 (97%)	40
MoO_3 hybrids	1 M H_2SO_4	135 F g^{-1} at 1.3 A g^{-1}	1000 (82%)	17
MoO_3/MWCNT	1 M $LiClO_4$ propylene carbonate	103 F g^{-1} at 25 mV s^{-1}	1000 (80%)	15
α-MoO_3 nanorods	1 M Na_2SO_4	214 F g^{-1} at 0.1 A g^{-1}	1000 (71.7%)	18

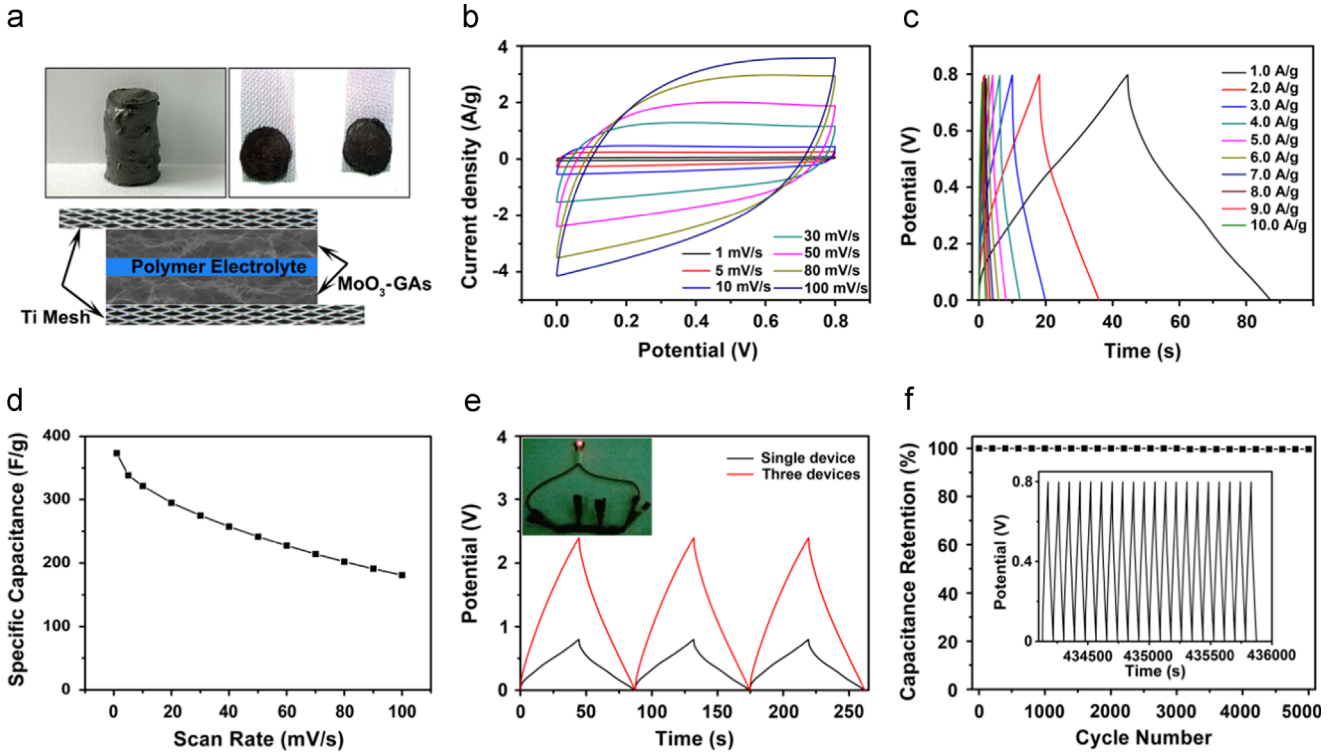

Figure 6 (a) Photographs of MoO_3-GAs monoliths and schematic diagram of a solid-state device with H_2SO_4-PVA polymer gel as the electrolyte. (b) CVs of a MoO_3-GAs based device at different scan rates. (c) Galvanostatic charge/discharge curves of a MoO_3-GAs based device at different current densities. (d) Specific capacitance of a MoO_3-GAs based device in a two-electrode system as a function of scan rate. (e) Galvanostatic charge/discharge curves at 1.0 A g^{-1} of a single solid-state supercapacitor (black curves) and three in series (red curves). Inset is a photograph of a red LED turned on by three devices in series. (f) Cycling stability of the MoO_3-GAs based device at a current density of 1.0 A g^{-1}. Inset shows the last 20 charge/discharge profile at 1.0 A g^{-1}.

features of the graphene oxide aerogels and the ultrathin MoO_3 nanocrystals.

The MoO_3-GAs based solid-state supercapacitors can be used to light a commercial red light-emitting diode (LED). Galvanostatic charge/discharge measurements showed that the potential window reached 0.8 V for a single device after being charged at 1 A g^{-1} for about 48 s; and when three devices of an equal mass loading were connected in series, the potential window reached 2.4 V (Figure 6e), which could easily light up a red LED after being fully charged, as manifested in the inset to Figure 6e. Electrochemical stability is another important property for practical applications of all-solid-state flexible supercapacitors. The performance durability was further evaluated using galvanostatic charge/discharge at a current density of 1.0 A g^{-1}. The device capacitance exhibited no obvious change even after 5000 charge/discharge cycles (Figure 6f).

Conclusions

In summary, we have described an effective strategy to prepare 3D supercapacitor electrodes based on the self-assembly of ultrathin MoO_3 nanocrystals on graphene oxide nanosheets. The layered structure between ultrathin MoO_3 nanocrystals and graphene nanosheets was fabricated via oxygen-bonding interactions at the interface, which facilitated charge transport in the perpendicular direction. Moreover, with abundant exposed active site of ultrathin MoO_3 nanocrystals and 3D porous graphene frameworks, the MoO_3-GAs composites exhibited rapid ion diffusion and electron transport, leading to a remarkable performance as electrode materials for supercapacitors. To our knowledge, the performance is the best among those reported in the literature with a high specific capacitances and excellent cycling stability in both aqueous (527 F g^{-1} at the current density of 1.0 A g^{-1}, 100% retention after 10,000 cycles) and solid electrolytes (373 F g^{-1} at 1.0 A g^{-1}, 100% retention after 5000 cycles). Such a remarkable performance is of significance in the design and fabrication of high-performance and long-lasting charge storage devices.

Acknowledgements

The authors thank Mr. Longji Shi for assistance in data processing. This work was supported by the National Recruitment Program of Global Experts, the PhD Start-up Funds of the Natural Science Foundation of Guangdong Province (S2013040016465), Zhujiang New Stars of Science & Technology (2014J2200061), and the Fundamental Research Funds for Central Universities (x2hjD2131690), China.

Appendix A. Supporting information

Supplementary data associated with this article can be found in the online version at http://dx.doi.org/10.1016/j.nanoen.2015.01.017.

References

[1] P. Simon, Y. Gogotsi, Nat. Mater. 7 (2008) 845.
[2] J.R. Miller, P. Simon, Science 321 (2008) 651.
[3] L.L. Zhang, X.S. Zhao, Chem. Soc. Rev. 38 (2009) 2520.
[4] H. Jiang, P.S. Lee, C. Li, Energy Environ. Sci 6 (2013) 41.
[5] Y. Wang, Y. Xia, Adv. Mater. 25 (2013) 5336.
[6] W.J. Zhou, K. Zhou, X.J. Liu, R. Hu, H. Liu, S.W. Chen, J. Mater. Chem. A 2 (2014) 7250.
[7] P. Yang, Y. Ding, Z. Lin, Z. Chen, Y. Li, P. Qiang, M. Ebrahimi, W. Mai, C.P. Wong, Z.L. Wang, Nano Lett. 14 (2014) 731.
[8] S. Chen, J. Zhu, X. Wu, Q. Han, X. Wang, ACS Nano 4 (2010) 2822.
[9] K.M. Hercule, Q. Wei, A.M. Khan, Y. Zhao, X. Tian, L. Mai, Nano Lett. 13 (2013) 5685.
[10] J. Zhu, L. Cao, Y. Wu, Y. Gong, Z. Liu, H.E. Hoster, Y. Zhang, S. Zhang, S. Yang, Q. Yan, P.M. Ajayan, R. Vajtai, Nano Lett. 13 (2013) 5408.
[11] W.J. Zhou, X.J. Liu, Y. Sang, Z. Zhao, K. Zhou, H. Liu, S.W. Chen, ACS Appl. Mater. Interfaces 6 (2014) 4578.
[12] K. Kalantar-zadeh, J. Tang, M. Wang, K.L. Wang, A. Shailos, K. Galatsis, R. Kojima, V. Strong, A. Lech, W. Wlodarski, R.B. Kaner, Nanoscale 2 (2010) 429.
[13] M.B. Sreedhara, H.S.S.R. Matte, A. Govindaraj, C.N.R. Rao, Chem. Asian J. 8 (2013) 2430.
[14] J. Chang, M. Jin, F. Yao, T.H. Kim, V.T. Le, H. Yue, F. Gunes, B. Li, A. Ghosh, S. Xie, Y.H. Lee, Adv. Funct. Mater. 23 (2013) 5074.
[15] Q. Mahmood, H.J. Yun, W.S. Kim, H.S. Park, J. Power Sources 235 (2013) 187.
[16] L.Q. Mai, B. Hu, W. Chen, Y.Y. Qi, C.S. Lao, R.S. Yang, Y. Dai, Z.L. Wang, Adv. Mater. 19 (2007) 3712.
[17] Q. Mahmood, W.S. Kim, H.S. Park, Nanoscale 4 (2012) 7855.
[18] Z. Cui, W. Yuan, C.M. Li, J. Mater. Chem. A 1 (2013) 12926.
[19] Y. Zhu, S. Murali, M.D. Stoller, K.J. Ganesh, W. Cai, P.J. Ferreira, A. Pirkle, R.M. Wallace, K.A. Cychosz, M. Thommes, D. Su, E.A. Stach, R.S. Ruoff, Science 332 (2011) 1537.
[20] L.L. Zhang, X. Zhao, M.D. Stoller, Y. Zhu, H. Ji, S. Murali, Y. Wu, S. Perales, B. Clevenger, R.S. Ruoff, Nano Lett. 12 (2012) 1806.
[21] Y. Yoon, K. Lee, C. Baik, H. Yoo, M. Min, Y. Park, S.M. Lee, H. Lee, Adv. Mater. 25 (2013) 4437.
[22] T. Kim, G. Jung, S. Yoo, K.S. Suh, R.S. Ruoff, ACS Nano 7 (2013) 6899.
[23] Y. Xu, K. Sheng, C. Li, G. Shi, ACS Nano 4 (2010) 4324.
[24] Y. Xu, Z. Lin, X. Huang, Y. Liu, Y. Huang, X. Duan, ACS Nano 7 (2013) 4042.
[25] H. Gao, F. Xiao, C.B. Ching, H. Duan, ACS Appl. Mater. Interfaces 4 (2012) 2801.
[26] P. Chen, J. Yang, S. Li, Z. Wang, T.Y. Xiao, Y.H. Qian, S.H. Yu, Nano. Energy 2 (2013) 249.
[27] H. Gao, F. Xiao, C.B. Ching, H. Duan, ACS Appl. Mater. Interfaces 4 (2012) 7020.
[28] F. Liu, S. Song, D. Xue, H. Zhang, Adv. Mater. 24 (2012) 1089.
[29] Z.S. Wu, A. Winter, L. Chen, Y. Sun, A. Turchanin, X. Feng, K. Müllen, Adv. Mater. 24 (2012) 5130.
[30] Y. Xu, Z. Lin, X. Huang, Y. Wang, Y. Huang, X. Duan, Adv. Mater. 25 (2013) 5779.
[31] W.S. Hummers, R.E. Offeman, J. Am. Chem. Soc. 80 (1958) 1339.
[32] H.L. Guo, P. Su, X. Kang, S.K. Ning, J. Mater. Chem. A 1 (2013) 2248.
[33] C.V. Subba Reddy, E.H. Walker Jr, C. Wen, S.-I. Mho, J. Power Sources 183 (2008) 330.
[34] S. Wang, Q. Gao, Y. Zhang, J. Gao, X. Sun, Y. Tang, Chem. Eur. J 17 (2011) 1465.
[35] Y. Dong, S. Li, H. Xu, M. Yan, X. Xu, X. Tian, Q. Liu, L. Mai, Phys. Chem. Chem. Phys. 15 (2013) 17165.
[36] Q. Huang, S. Hu, J. Zhuang, X. Wang, Chem. Eur. J 18 (2012) 15283.
[37] T. Brezesinski, J. Wang, S.H. Tolbert, B. Dunn, Nat. Mater. 9 (2010) 146.
[38] G. Zhou, D.W. Wang, L.C. Yin, N. Li, F. Li, H.M. Cheng, ACS Nano 6 (2012) 3214.
[39] G.R. Li, Z.L. Wang, F.L. Zheng, Y.N. Ou, Y.X. Tong, J. Mater. Chem. 21 (2011) 4217.
[40] E.G. da SilveiraFirmiano, A.C. Rabelo, C.J. Dalmaschio, A.N. Pinheiro, E.C. Pereira, W.H. Schreiner, E.R. Leite, Adv. Energy Mater 4 (2014).
[41] P. Meduri, E. Clark, J.H. Kim, E. Dayalan, G.U. Sumanasekera, M.K. Sunkara, Nano Lett 12 (2012) 1784.
[42] Z.S. Wu, Y. Sun, Y.Z. Tan, S. Yang, X. Feng, K. Müllen, J. Am. Chem. Soc. 134 (2012) 19532.
[43] D. Hanlon, C. Backes, T.M. Higgins, M. Hughes, A. O'Neill, P. King, N. McEvoy, G.S. Duesberg, B. Mendoza Sanchez, H. Pettersson, V. Nicolosi, J.N. Coleman, Chem. Mater. 26 (2014) 1751.
[44] Z.S. Wu, A. Winter, L. Chen, Y. Sun, A. Turchanin, X. Feng, K. Müllen, Adv. Mater. 24 (2012) 5130.
[45] Y. Xu, Z. Lin, X. Huang, Y. Wang, Y. Huang, X. Duan, Adv. Mater. 25 (2013) 5779.

Kai Zhou is currently pursuing a Ph.D. under the supervision of Dr. Weijia Zhou and Prof. Shaowei Chen in the School of Environment and Energy at the South China University of Technology, China. His research is focused on the designs and synthesis of nanomaterials for energy conversion and storage.

Weijia Zhou completed his Ph.D. with Prof. Hong Liu and Prof. Jiyang Wang at Shandong University in 2012. He was doing research in Prof. Hua Zhang's group at Nanyang Technological University in 2011. Now, he is working in New Energy Research Institute, School of Environment and Energy, South China University of Technology, China. His research interests are related to the designs and synthesis of low dimensional nanomaterials for energy conversion and storage, including photo and electro-catalytic water splitting, and supercapacitor.

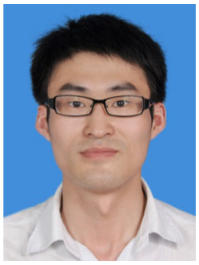

Xiaojun Liu is pursuing Ph.D. under the supervision of Prof. Shaowei Chen at the School of Chemistry and Chemical Engineering, South China of Technology University, China. He acquired his MS from the Shaanxi Normal University in 2009 working on the development of novel carbon materials for energy storage (supercapacitors). Currently, his research is focused on the design and synthesis of porous materials and nanostructured materials for applications in catalysis and energy storage.

Yuanhua Sang obtained his Ph.D. with Prof. Hong Liu at Shandong University in 2012. He was working with Dr. Dehong Yu at Bragg Institute of Australian Nuclear Science and Technology Organisation from 2011 to 2012. Now, he works as a lecturer in State Key Laboratory of Crystal Materials, Shandong University, China. His research interests are structure and property investigation of inorganic crystal materials with neutron and x-ray diffraction; structural or functional materials by routes of single crystal growth and ceramic procedure; materials for solar light conversion including the photocatalytic environmental purification and energy storage by water splitting.

Shaozheng Ji is currently a master student of Materials Physics and Chemistry at Shandong University under the supervision of Prof. Hong Liu. He obtained his B.S. degree in Materials Physics at Shandong University, China in 2012. His current research interest focuses on the synthesis of one-dimensional metal oxide semiconductors and their application for photodetector and gas sensor.

Wei Li is currently pursuing a master's degree under the supervision of Prof. Shaowei Chen in the School of Environment and Energy at the South China University of Technology, China. His research is focused on the synthesis of conductive organic films for solar cells and gas sensor.

Jia Lu is currently pursuing a Master under the supervision of Dr. Weijia Zhou and Prof. Shaowei Chen in the school of Environment and Energy at South China University of Technology, China. Her research is focused on the synthesis of nanomaterials as electrocatalyst for oxygen reduction reaction.

Ligui Li obtained a B.Sc. degree from Jilin University in 2004 and received Ph.D. degree from Changchun Institute of Applied Chemistry, Chinese Academy of Sciences in 2010. He then started postdoctoral research in collaboration with Professor Hai-feng Ji at Drexel University in 2010 and Professor Ling Zang at the University of Utah in 2011, respectively. In 2013, he became an associate professor of the College of Environment and Energy at South China University of Technology. His recent research interests include organic/polymer opto-electronic materials, preparation of high performance organic/polymer solar cells and perovskite solar cells, and nanomaterials for electrochemical applications.

Wenhan Niu received his Master's degree from Wuhan University of Technology in 2012 and he is pursuing his Ph.D. degree under the supervision of Prof. Shaowei Chen in electrochemistry and novel functional nanomaterials in South China University of Technology. He is interested in organometal halide perovskites solar cells, highly conducting materials for organic electronics and electrochemical applications

Hong Liu is professor in State Key Laboratory of Crystal Materials, Shandong University, and adjunct professor in Beijing Institute of Nanoenergy and Nanosystem, CAS. He has published over 250 peer reviewed paper, such as, Adv. Mater., J. Am. Chem. Soc., Nano Letters, etc., and published more than 25 patents. He was awarded as Distinguished Young Scholar by NNSF and Professor of Hundred Talents Program of CAS. His current research is focused mainly onnonlinear crystal growth, chemical processing of nanomaterials for energy related applications including photocatalysis, tissue engineering, especially the interaction between stem cell and nanostrucuture of biomaterials.

Shaowei Chen obtained a B.Sc. degree from the University of Science and Technology of China, and then went to Cornell University receiving his M.Sc. and Ph.D. degrees in 1993 and 1996. Following a postdoctoral appointment in the University of North Carolina at Chapel Hill, he started his independent career in Southern Illinois University in 1998. In 2004, he moved to the University of California at Santa Cruz and is currently a Professor of Chemistry. He is also an adjunct professor at South China University of Technology. His research interest is primarily in the electron transfer chemistry of nanoparticle materials.